Temperature- and pressure-dependent lattice behaviour of $RbFe(MoO_4)_2$

2010 J. Phys.: Condens. Matter 22 055406

(http://iopscience.iop.org/0953-8984/22/5/055406)

J. Phys.: Condens. Matter **22** (2010) 055406 (10pp) doi:10.1088/0953-8984/22/5/055406

Temperature- and pressure-dependent lattice behaviour of $RbFe(MoO_4)_2$

A Waśkowska[1], L Gerward[2], J Staun Olsen[3], W Morgenroth[4], M Mączka[1] and K Hermanowicz[1]

[1] Institute of Low Temperature and Structure Research, Polish Academy of Sciences, PL-50 422 Wrocław, Poland
[2] Department of Physics, Technical University of Denmark, DK-2800 Lyngby, Denmark
[3] Niels Bohr Institute, Oersted Laboratory, University of Copenhagen, DK-2100 Copenhagen, Denmark
[4] c/o Desy/Hasylab, D-22607 Hamburg, Germany

E-mail: A.Waskowska@int.pan.wroc.pl

Received 17 June 2009, in final form 10 December 2009
Published 19 January 2010
Online at stacks.iop.org/JPhysCM/22/055406

Abstract

Trigonal $RbFe(MoO_4)_2$ is a quasi-two-dimensional antiferromagnet on a triangular lattice below $T_N = 3.8$ K, The crystal exhibits also a structural phase transition at $T_c = 190$ K related to symmetry change from $P\bar{3}m1$ to $P\bar{3}$. We present the temperature- and pressure-dependent characteristics of this material in the context of ambiguous opinions on the symmetry and crystal properties below T_c. A single-crystal x-ray diffraction shows that the temperature-dependent evolution of the unit cell in the range 100–300 K is strongly anisotropic with markedly discontinuous changes at T_c. The transition is connected with a spontaneous strain developing in effect of the volume decrease. The structure releases the strain by rotation of corner-sharing rigid MoO_4 and FeO_6 polyhedra in the (a, b) basal plane. The temperature dependence of the IR vibrational wavenumbers exhibits weak changes near T_c, which are consistent with the symmetry transformation from $P\bar{3}m1$ to $P\bar{3}$. High-pressure x-ray powder diffraction indicates that the material is extremely soft but with some stiffening at high pressure. The zero-pressure bulk modulus is $B_0 = 7.9(6)$ GPa and the pressure derivative is $B_0' = 10(1)$. The compression curve can be described by a single equation of state, corresponding to the trigonal cell, up to 5 GPa. An amorphization appearing above 5 GPa and increasing gradually on further pressure increase suggests the thermodynamic instability of the high-pressure structure.

(Some figures in this article are in colour only in the electronic version)

1. Introduction

$RbFe(MoO_4)_2$ belongs to the group of magnetic solids of composition $AM(XO_4)_2$, where A is an alkali metal, M = Cr^{3+}, Mn^{3+} or Fe^{3+}, and X = Mo, W, S or Se [1, 2]. These compounds exhibit various physical properties connected with polymorphism of their layered trigonal structures and triangular-lattice magnetic phases [3–6]. Although $RbFe(MoO_4)_2$ has been investigated for a long time, it is still attracting attention since new phenomena connected with multiferroicity have lately been revealed by Kenzelmann *et al* [7]. Multiferroics are especially important as they offer a wide range of new applications. Due to the potential for tuning the magnetic properties with an external electric field and, conversely, by setting the dielectric properties as a function of the magnetic field, numerous multifunctional materials can be obtained.

The crystal structure of $RbFe(MoO_4)_2$ (abbreviated to RFMO) has been shown to be isotypic with $KAl(MoO_4)_2$, which has space group $P\bar{3}m1$ [1, 2]. In this structural type the magnetic ions, which are substituting Al^{3+}, are located in triangular nets, stacked in separated layers. Bazarov *et al* [8] have synthesized single crystals of RFMO and determined their structure by x-ray diffraction at room temperature. The structure, which was subsequently confirmed by Wierzbicka-Wieczorek *et al* [9], is built of FeO_6 octahedra sharing vertices

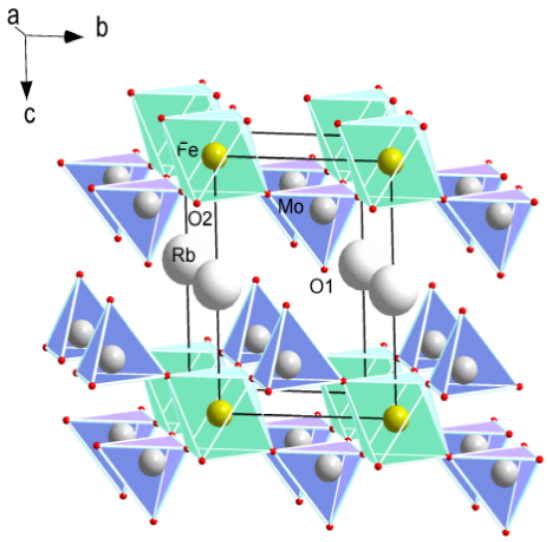

Figure 1. The crystal structure of $RbFe(MoO_4)_2$ at room temperature.

with MoO_4 tetrahedra. Together they form layers arranged perpendicular to the c axis, the Rb atoms occupying the interlayer space (figure 1).

The magnetic properties of RFMO, due to Fe^{3+} ions with spin $S = 5/2$, were first investigated by Inami *et al* [4], based on high-field magnetization measurements. The data showed a one-third magnetization plateau, specific for quasi-two-dimensional triangular-lattice antiferromagnets. Their spins rotate by 120° in the $(a \times b)$ basal plane forming a three-sublattice structure, while along the c axis the spin alignment is approximately antiparallel. Further studies by single-crystal electron spin resonance (ESR) and magnetization [10, 11], together with external field-dependent specific heat measurements [12], allowed the construction of the high-temperature $(H–T)$ phase diagram containing a sequence of field-induced phase transitions below the Néel temperature T_N. It was established that, in the absence of the external magnetic field, RMFO undergoes a phase transition at $T_N = 3.8$ K with non-collinear spin order confined to the basal plane, while a field between 4.7 and 7.1 T applied in-plane induces collinear spin alignment, causing the magnetization plateau at one-third of the saturation moment. Additionally, a first-order phase transition in a field of 3.5 T and governed by a weak interplanar exchange was reported but its nature was not explained [10].

RFMO exhibits another interesting property, namely a structural phase transition at $T_c = 190$ K. It was revealed by electron spin resonance (ESR), Raman spectroscopy and powder x-ray diffraction (XRD) [13]. The anomalous scattering behaviour was associated with a change of the $P\bar{3}m1$ crystal symmetry to $P\bar{3}c1$, but the resolution of the XRD diagrams was too low to allow a symmetry determination of this phase. Based on a neutron powder diffraction analysis, it was lately concluded by Inami *et al* [14] that $RbFe(MoO_4)_2$ is a classical Heisenberg antiferromagnet with weak XY anisotropy in the basal plane and incommensurate antiferromagnetic stacking along the c axis.

Furthermore, it was shown in [14] that the structural phase transition at $T_c = 190$ K is connected with the symmetry change to $P\bar{3}$.

Recent studies on spin–phonon interactions in frustrated magnets suggest that, besides the known multiferroics like $Ni_3V_2O_8$ [15] and perovskite-type manganites $ReMnO_3$ [16], the present crystal may exhibit ferroelectric spontaneous polarization induced by incommensurate modulated long-range antiferromagnetic order below T_N [7]. Kenzelmann *et al* [7] have shown that ferroelectricity in RFMO can be observed when, in the triangular Fe^{3+} sublattice, the spin arrangement in the magnetic structure is chiral. The inversion symmetry is then broken. The ferroelectric order coupled with the magnetic order appears as a secondary effect (improper ferroelectricity).

While the magnetic characteristics of RFMO are extensively studied, little is known about the precise crystal behaviour below the structural phase transition at $T_c = 190$ K. In the present report we attempt to determine the properties of this phase in more detail, especially in the context of ambiguous opinions on the symmetry of the phase formed below T_c. For this purpose, we have measured the temperature evolution of the unit-cell parameters in the range 100–300 K, using high-resolution single-crystal x-ray diffraction and synchrotron radiation. Moreover, the single-crystal structure has been re-determined at room temperature and at 110 K, using a conventional x-ray source, in order to find out how the structural units are involved in the mechanism of the phase transition. Some additional information on structural changes occurring during the transition has also been obtained from the temperature-dependent infrared (IR) studies performed in the 5–295 K range. Independently, we have studied the high-pressure structural stability using energy-dispersive powder x-ray diffraction in conjunction with the diamond-anvil cell and synchrotron radiation.

2. Experimental details

Single crystals of $RbFe(MoO_4)_2$ were grown by a flux method described in [1]. A mixture of Rb_2CO_3, Fe_2O_3 and MoO_3 (Fluka products) in a ratio 2:1:6 was placed in a platinum crucible, heated to 800 °C and kept at this temperature for 40 h. Next, the melt was cooled at a rate of 2 °C h^{-1} to 500 °C and then cooled at a rate of 5 °C h^{-1} to room temperature. Light-yellow-green transparent crystals of plate-like shape were extracted from the crucible by washing in hot water. Their chemical composition was checked using a microprobe analyzer (Philips SEM 515) and an EDAX spectrometer (Philips PV 9800).

A sample with dimensions given in table 1 was selected for single-crystal x-ray diffraction. The evolution of the unit-cell parameters with decreasing temperature was studied at station D3 of the Hamburg Synchrotron Radiation Laboratory (HASYLAB), using a Huber four-circle diffractometer with a point detector. The wavelength was adjusted to $\lambda = 0.7000$ Å. Low temperatures in the range 100–300 K were obtained using an Oxford Cryojet based on liquid nitrogen. At each temperature, the unit-cell parameters were calculated by a

Table 1. Crystal data and experimental details for $RbFe(MoO_4)_2$ at room temperature and 110 K.

Temperature (K)	295	110
Space group	$P\bar{3}m1$ (#164)	$P\bar{3}$ (#147)
Lattice parameters (Å)		
a	5.6694(4)	5.607(3)
c	7.4922(7)	7.452(6)
γ	120	120
V/Z	208.55(1)/1	202.9(1)/1
Density (calculated) (g cm^{-3})	3.672	3.774
μ (Mo Kα) (mm^{-1})	10.48	10.77
Crystal size (mm^3)	0.12 × 0.12 × 0.09	0.12 × 0.12 × 0.09
Maximum 2θ (deg)	90.44	88.22
Index ranges:		
h	−11, +11	−9, +9
k	−11, +11	−10, +6
l	0, 14	−8, +14
Reflections collected	2578	3836
Independent reflections, R_{int}	695/0.034	962/0.019
Data/parameters	572/18	907/21
Extinction correction	0.156(5)	0.021(1)
Final R indices [$I > 2\sigma(I)$]		
R_1; $/R$ (all)	0.026/0.035	0.019/0.021
wR_2	0.052	0.045
Goodness of fit on F^2	1.093	1.005
Minimum and max $\Delta\rho$(eÅ^{-3})	−1.99, +1.99	−1.03, +1.11

least-squares refinement using the setting angles of 24 high-angle Bragg reflections with $2\theta \approx 75°$.

Diffraction data for crystal structure determination at 300 and 110 K were collected with the KM-4 *Xcalibur* single-crystal diffractometer equipped with a CCD detector (Oxford Diffraction) and operated in κ geometry. The laboratory x-ray source of graphite-monochromated Mo Kα radiation was used. Data were collected in ω-scan mode with $\Delta\omega = 1.0°$ from a fresh sample of dimensions given in table 1. About 1150 images were recorded in nine runs with different angular settings and for an exposure time of 30 s/image. The diffraction data were integrated for intensities and corrected for Lorentz polarization effects using the *CrysAlis* program package [17]. The absorption correction was applied with the Gaussian face-indexed numerical routine [18]. Structure solution at room temperature and 110 K was carried out using direct methods. Subsequent refinements based on F^2 data were made with the *SHELXL97* program system [19]. Crystal data, experimental details and parameters for the structural refinement at room temperature and 110 K are summarized in table 1.

Room-temperature, high-pressure powder x-ray diffraction (XRD) patterns were recorded at station F3 of HASYLAB–DESY, using the white-beam method and synchrotron radiation. The diffractometer, working in the energy-dispersive mode, has been described elsewhere [20]. High pressures were obtained in a diamond-anvil cell of Syassen–Holzapfel type. A finely ground powder sample and a ruby chip as a pressure marker were placed in a hole with diameter 200 μm in an Inconel gasket, pre-indented to a thickness of 60 μm. A 16:3:1 methanol:ethanol:water mixture was used as the pressure-transmitting medium. The pressure was determined by the ruby luminescence method, using the nonlinear pressure scale of Mao *et al* [21]. The Bragg angle of each run was calculated from a zero-pressure spectrum of sodium chloride (NaCl) in the diamond-anvil cell.

Temperature-dependent IR spectra were measured with a Biorad 575 FT-IR spectrometer in KBr suspension for the 1200–400 cm^{-1} region and in Nujol suspension for the 500–40 cm^{-1} region. Low temperature was obtained using a helium-flow Oxford cryostat.

3. Results and discussion

3.1. Thermal expansion

The evolution of the unit cell as a function of temperature at ambient pressure is shown in figure 2. The cell appears strongly temperature-dependent and anisotropic. The high resolution of the synchrotron radiation method allows us to observe that a continuous strain begins to develop on cooling from RT and saturates at about 190 K. Pronounced discontinuities at that temperature indicates that the strain is relieved by a structural phase transition reported in [11–13]. At the first stage of cooling, the length of the a axis is nearly stable, while the c axis becomes linearly contracted, meaning that between room temperature and T_c, the changes in crystal volume are mainly related to a decrease of the distances between Rb^+ and rigid polyhedral layers built of the corner-shared MoO_4 and FeO_6 anionic groups (cf figure 1). On cooling below T_c, the changes in the crystallographic c direction become relatively small, but those in the ($a \times b$) plane, connected with a deformation in the polyhedral layer itself, appear essential. This behaviour is compatible with the layer-like structure shown in figure 1.

The character of the volume change suggests a weak first-order transition. The thermal expansion coefficients calculated over the two temperature ranges are given in table 2. The

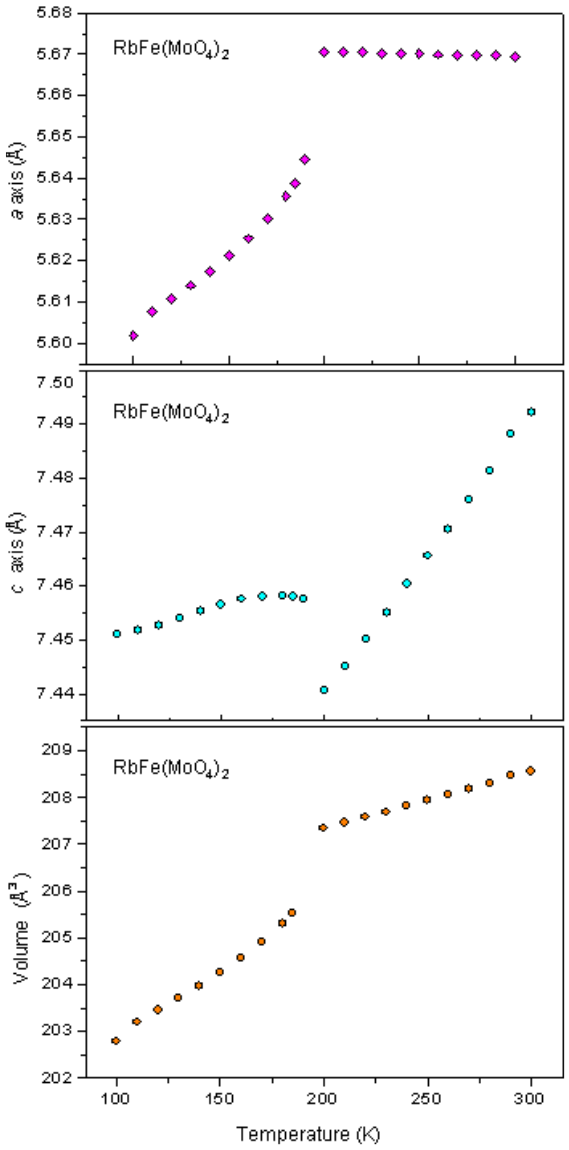

Figure 2. Temperature dependence of the unit-cell parameters for $RbFe(MoO_4)_2$.

Table 2. Linear and volume thermal expansion coefficients α_i and β ($\times 10^{-5}$ K^{-1}) calculated over the two ranges, corresponding to the temperatures above and below $T_c = 190$ K. ($\alpha_i = \Delta a_i/(a_i \Delta T)$.)

T range (K)	α_a	α_c	β
200–300	−0.49	6.90	5.84
110–190	8.44	0.95	15.18

volume expansion coefficient $\beta = \Delta V/(V_0 \Delta T)$ is 1.38×10^{-4} K^{-1} in the whole measured range 100–300 K, showing that the crystal is soft and that the cell contracts by 2.8%.

In order to see in more detail the geometry of the resulting structural groups, the two phases are compared and the mechanism of the transition is discussed in sections 3.2 and 3.3.

3.2. Room-temperature structure

Re-determination of the RT structure confirmed previous results [8–14]. Atomic positions and thermal displacement amplitudes are given in table 3. The projection of the structure viewed along the c axis is shown in figure 3(a). The regular FeO_6 octahedron shares all six corners with MoO_4 tetrahedra, forming a polyhedral layer. As the tetrahedron shares only three of its four vertices, a lone electron pair is localized at the free apex O1 atom. Table 4 shows that the Mo–O1 distance is significantly shorter than the three other distances, and that the distorted tetrahedral angles range from 107.70(7) to 111.18(6)°. The apices of the neighbouring tetrahedra in the unit cell point in opposite directions along the c axis. Each Rb cation located between the layers is coordinated with symmetry-equivalent six O1 and six O2 atoms at the distances 3.018(2) and 3.2883(4) Å, respectively.

Table 3. Fractional atomic coordinates and equivalent isotropic displacement parameters ($10^3 \times$ Å^2) for $RbFe(MoO_4)_2$. In the first row are given the room-temperature data in $P\bar{3}m1$, and in the second row the 110 K data in $P\bar{3}$.

Atom	Site	x	y	z	U_{eq}
Mo	2d	0.3333	0.6667	0.229 30(4)	10.4(1)
		0.3333	0.6667	0.230 86(3)	4.8(5)
Fe	1a	0.0	0.0	0.0	10.5(1)
		0.0	0.0	0.0	5.10(8)
Rb	1b	0.00	0.0	0.5	24.9(1)
		0.0	0.0	0.5	9.7(1)
O1	2d	0.3333	0.6667	0.458 0(4)	25.7(6)
		0.3333	0.6667	0.461 4(3)	10.8(3)
O2	6i	0.1620(2)	0.3241(4)	0.157 7(2)	28.8(4)
	6g	0.1127(4)	0.3233(3)	0.158 5(2)	11.9(3)

Table 4. Selected interatomic distances (Å) and angles (deg) for (a) $RbFe(MoO_4)_2$.

Distance	290 K	110 K
Mo–O1	1.713(3)	1.717(3)
Mo–O2	1.766(2) × 3	1.774(2)
Fe–O2	1.981(2) × 6	1.984(2)
Rb–O1	3.2883(4) × 6	3.250(4)
Rb–O2	3.018(2) × 6	3.003(3)
Fe–Rb	3.7461(4)	3.726(4)
Mo–Rb	3.8506(3)	3.808(2)
$O2–O2_{short}$	2.848(7)	2.849(2)
$O2–O2_{long}$	2.913(5)	2.927(2)
Angle		
O1–Mo–O2	107.70(7)	107.70(6)
O2–Mo–O2	111.18(6)	111.18(6)
O2–Fe–O2	91.89(8)	91.81(9)
Fe–O2–Mo	161.1(1)	154.6(1)9

3.3. Low-temperature structure at 110 K

The neutron powder diffraction data discussed by Inami [14] have shown that at 15 K the symmetry of RFMO is $P\bar{3}$. However, the structural analogy with the isotypic $KAl(MoO_4)_2$ leads to ambiguous opinions regarding the symmetry of the low-temperature phase [13]. Therefore, in the structural calculations based on x-ray diffraction, the space groups $P3m1$, $P321$, $P\bar{3}$ and $P\bar{3}c$ suggested in the literature have also been considered. Space group $P3m1$ was rejected because of strong correlations between the positional parameters of

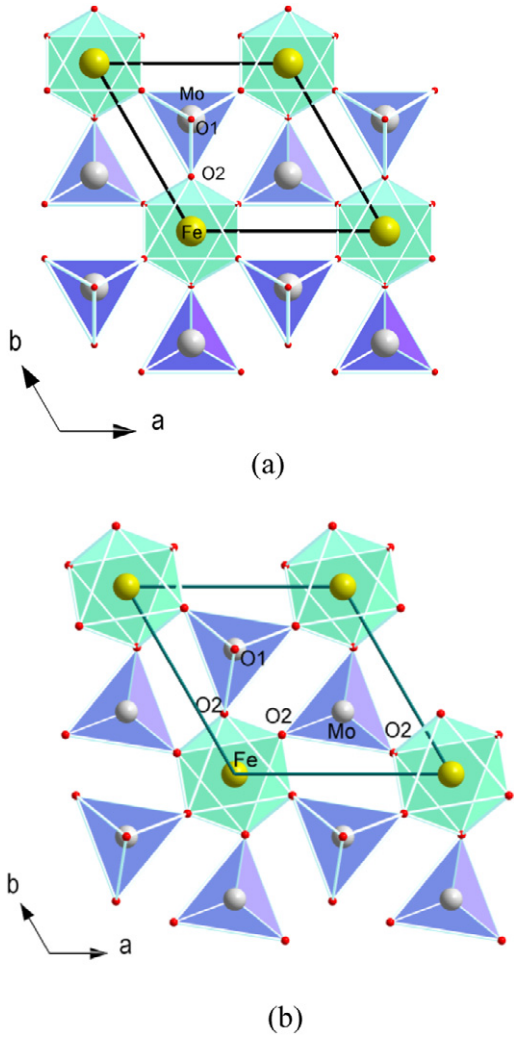

Figure 3. Polyhedral projection of the structure viewed along the *c* axis: (a) at the room-temperature phase and (b) at 110 K (space group $P\bar{3}$).

four symmetrically independent O atoms and the unreasonably small value of the thermal displacement of the O atom at the Wyckoff position 3d. For $P321$ a statistical test for space group determination on the reflection intensities was ambiguous and a proper structural model could not be constructed. The $P\bar{3}c$ space group would require a doubling of the *c* axis and space group extinctions $h\bar{h}0l$ for $l = 2n+1$, which were not observed in the intensity dataset. The best fit was obtained for $P\bar{3}$, consistent with the results of [14]. The atomic positions and thermal displacement amplitudes obtained in the present study are given in table 3.

The evolution of the unit-cell parameters with temperature of the first sample, as well as the intensity statistic tests of the second sample chosen for the structural determination, evidently pointed to a twinned state of these crystals, which was difficult to observe at room temperature [22]. The twin domains were related by a twofold axis parallel to the *b* axis and the twin operation was $(-1\,-1\,0, 0\,1\,0, 0\,0\,-1)$. The effect was taken into account with the *Twin Refinement* procedure implemented in the SHELXL'97 program [19]. It was assumed

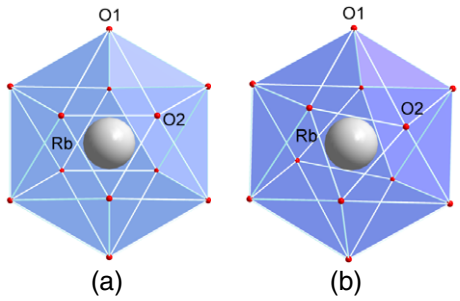

Figure 4. Coordination polyhedron of Rb^+ before and after the phase transition at 190 K.

that the two individuals contribute to the diffracted intensities in the same proportion.

The symmetry of the mirror plane pertaining to all Wyckoff positions at RT is lost as a result of the phase transition (table 3). Nevertheless, the location of Fe^{3+} at (0 0 0) remains unchanged and it forms a regular FeO_6 octahedron, while Mo at $(0, 0, z)$ is free to move along the threefold axis. A comparison of the structural model at RT and 110 K is shown in projection along the *c* axis (figures 3(a) and (b)). Due to the cell contraction the interlayer spacing decreases, as both the Rb–Mo as well as Rb–Fe distances are evidently shorter than they were at RT (table 4).

It was expected that the Rb cation, situated between the polyhedral layers, should play a role in the phase transition mechanism because it is the most weakly bonded atom in the structure, and it could easily be displaced from its high-symmetry position, breaking thereby the inversion symmetry of the phase. It appears, however, that Rb^+ remains at the 0 0 1/2 site, but the six O2 atoms of the Rb^+ coordination polyhedron are forced away from their RT positions. The effect is illustrated in figure 4, showing the shape of the coordination icosahedron before and after the transition. The O2 atoms' displacements cause the in-phase rotations of the rigid MoO_4, entailing also rotations of FeO_6, which results in deformation of the polyhedral framework (figure 3). The Fe–O2–Mo angle and the shape of interpolyhedral parallelograms with short and long distances between two symmetry equivalent O2–O2 atoms define the framework. These parameters are essentially different from those at room temperature (cf table 4). Inspection of the anisotropic displacement parameters (ADP) shows that all U_{ij} components are much lower at 110 K than at RT, implying stronger interatomic interactions at low temperatures (table 5).

The structure may be treated as a quasi-two-dimensional system, the spacing of the layers being determined by the length of the *c* axis (≈7.4 Å). During the compression, various paths of indirect spin exchange via O atoms in the basal plane and in the *c* direction become changed [3, 14, 23]. The strength of the superexchange of the type Fe–O2–O2–Fe, where two oxygen atoms in the basal plane are involved, is more sensitive to the bond angle than to the bond length [23]. Comparison of the geometry of the polyhedral chain at 110 K and RT (figures 3(a) and (b)) shows that the angles within the interpolyhedral parallelograms built by the long and short O2–O2 edges are 100.63(2) and 79.37(2)°, differing considerably

Table 5. The anisotropic displacement amplitudes U_{ij} ($10^2 \times$ Å^2) for $RbFe(MoO_4)_2$. In the first row are given the room-temperature data in $P\bar{3}m1$ and in the second row the 110 K data in $P\bar{3}$.

Atom	U_{11}	U_{22}	U_{33}	U_{23}	U_{13}	U_{12}
Mo	0.979(9)	0.979(9)	1.16(12)	0.0	0.0	0.490(5)
	0.490(6)	0.490(6)	0.450(8)	0.0	0.0	0.245(3)
Fe	0.84(2)	0.84(2)	1.49(3)	0.0	0.0	0.418(8)
	0.48(1)	0.48(1)	0.56(2)	0.0	0.0	0.24(06)
Rb	3.01(2)	3.01(2)	1.48(2)	0.0	0.0	1.50(1)
	1.19(1)	1.19(1)	0.54(1)	0.0	0.0	0.59(05)
O1	3.2(1)	3.2(1)	1.3(1)	0.0	0.0	1.60(5)
	1.27(6)	1.27(6)	0.71(7)	0.0	0.0	0.63(3)
O2	3.29(8)	1.55(7)	3.06(9)	−0.99(7)	−0.50(3)	0.77(4)
	1.45(7)	0.93(6)	1.04(5)	−0.21(05)	0.00(4)	0.47(5)

from right angles at RT (table 4). The lattice compression in the *c* direction may also enhance the weaker interlayer couplings realized via three or more O atoms along the paths of the type Fe–O–Mo–O–Fe.

It can thus be concluded that the mechanism of the transition is related to the geometrical frustration and resulting spontaneous strain arising as an effect of the volume contraction. The structure relieves that strain by the distortions in the polyhedral layer following the O2 atom displacements. Therefore, the phase below T_c is of a ferroelastic nature.

3.4. Temperature-dependent infrared spectroscopy

The study was undertaken in order to show consistency with the neutron and x-ray diffraction results. Group theory predicts the existence of 33 optical vibrations distributed among the $4A_{1g} + A_{2g} + 5E_g + 1A_{1u} + 5A_{2u} + 6E_u$ Brillouin zone centre modes of $RbFe(MoO_4)_2$ in space group $P\bar{3}m1$. These modes can be subdivided into symmetric stretching ($A_{1g} + A_{2u}$), asymmetric stretching ($A_{1g} + E_g + A_{2u} + E_u$), symmetric bending ($E_g + E_u$), asymmetric bending ($A_{1g} + E_g + A_{2u} + E_u$), librational ($A_{2g} + E_g + A_{1u} + E_u$) and translational ($A_{1g} + E_g$) modes of the MoO_4^{2-} ions; translational ($A_{2u} + E_u$) modes of the Rb^+ ions; and coupled translations ($A_{2u} + E_u$) of the Fe^{3+} and MoO_4^{2-} ions. Among these modes the A_{1g} and E_g modes are Raman-active, the A_{2u} and E_u modes are IR-active, whereas the A_{2g} and A_{1u} modes are both IR- and Raman-inactive. This analysis shows that 11 modes are expected in the infrared range and 9 modes in the Raman spectra of $RbFe(MoO_4)_2$.

The room-temperature IR spectrum of $RbFe(MoO_4)_2$ is given in figure 5. The bands originating from the fundamental transitions are readily identified by comparison with spectra of other trigonal molybdates previously studied by us [24–26]. Thus, the totally symmetric stretching mode is observed as a weak band near 952 cm^{-1}. The most intense band near 824 cm^{-1} and a medium intensity band near 921 cm^{-1} correspond to the E_u and A_{2u} asymmetric stretching modes, respectively. In the low wavenumber region, the five most intense bands are observed at 388, 326, 302, 256 and 235 cm^{-1}. The corresponding bands of the alkali-metal aluminium and scandium double molybdates were observed at higher wavenumbers (505–295 and 407–266 cm^{-1}, respectively [24–26]). This result clearly shows that the wavenumbers of these bands decrease significantly

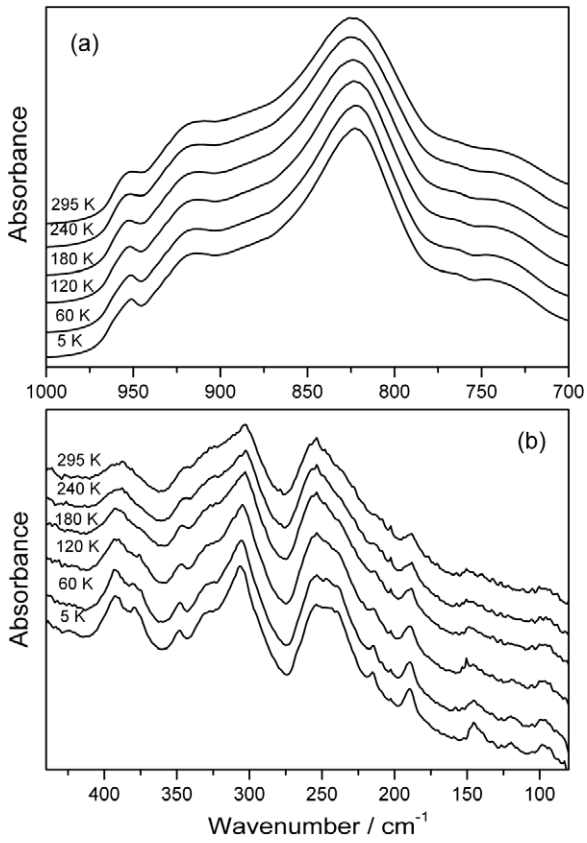

Figure 5. Spectra at selected temperatures in the mid-IR (a) and far-IR (b) region.

with increasing mass of the trivalent ion. Therefore, we assign these bands to coupled modes involving bending vibrations of MoO_4^{2-} as well as translations of the MoO_4^{2-} and Fe^{3+} ions. Moreover, the far-IR spectrum shows three weak bands at 188, 150 and 98 cm^{-1}. The band at 188 cm^{-1} can most likely be assigned to the librational mode of the MoO_4^{2-} ions because a similar librational band was observed for the alkali-metal aluminium double molybdates at 167–175 cm^{-1} [26]. The two remaining bands originate from the translational motion of the Rb^+ ions. Apart from these fundamental transitions, there are also clear bands at 735 and 345 cm^{-1}; which can probably be assigned to overtones or combination bands.

Having obtained a clear picture of the vibrational properties of $RbFe(MoO_4)_2$ in space group $P\bar{3}m1$, we next

consider the effects of temperature on the vibrational properties of this compound. According to the single-crystal x-ray data discussed above, the best fits were found for the $P\bar{3}$ symmetry. Our former studies of ferroelastic phase transitions in trigonal $KAl(MoO_4)_2$ and $KIn(WO_4)_2$ showed that a monoclinic distortion can be very clearly observed in the IR and Raman spectra through splitting of doubly degenerate bands [26, 27]. In particular, as a result of symmetry decrease, a new IR band appeared at the low wavenumber side of the most intense IR band attributed to the E_u mode in the trigonal phase. Moreover, a very clear splitting of the symmetric bending mode was observed in the Raman spectra. Since we do not observe any splitting of the 824 cm^{-1} IR band down to $T = 5$ K (figure 5), and also no splitting of Raman modes was observed by Klimin *et al* [13], the $C2/m$ space group can be excluded for the low-temperature phase of $RbFe(MoO_4)_2$. Vibrational spectra, therefore, prove that the low-temperature structure remains trigonal.

The low-temperature $P\bar{3}$ structure has the same number of formula units in the primitive cell as the high-temperature $P\bar{3}m1$ structure. As a result of the phase transition, the site symmetries of Fe, Rb, Mo, O1 and O2 decrease from D_{3d}, D_{3d}, C_{3v}, C_{3v} and C_s to C_{3i}, C_{3i}, C_3, C_3 and C_1, respectively. As a consequence, all IR-active A_{2u} and silent A_{1u} modes of the $P\bar{3}m1$ structure become IR-active A_u modes of the $P\bar{3}$ structure, whereas the doubly degenerate modes have the same symmetry in both structures (E_u). Therefore, the number of IR-active modes does not change for the internal and translational vibrations. The only difference is expected for the silent A_{1u} librational mode of the $P\bar{3}m1$ structure, which should become infrared-active in the $P\bar{3}$ structure.

Our results show that temperature-dependent changes in the IR spectra are very weak (figure 5), in agreement with the expected symmetry change. The linewidth decreases with decreasing temperature and therefore some weaker bands are better resolved at low temperatures. Our calculations performed for alkali-metal aluminium molybdates showed that the Raman-and IR-inactive A_{1u} librational mode should be observed at higher wavenumbers than the E_u librational mode [26]. In the low-temperature IR spectra a weak band is observed at about 214 cm^{-1}, which could be attributed to the A_{1u} librational mode activated in the $P\bar{3}$ structure. However, this band seems to be already present at 240 K and therefore it is likely that it should be attributed to an overtone or a combination, rather than to the librational mode. Another band, which can clearly be observed at 5 K, is that at 379 cm^{-1}. This band is also present above the phase transition temperature, as shown by the strongly asymmetric shape of the contour in the 360–410 cm^{-1} range, and it appears clearly at low temperatures due to a decrease of phonon damping. The origin of this band is not clear but it is likely that it also corresponds to an overtone or a combination band. In figure 5 a weak band also appears at about 122 cm^{-1}. Although its wavenumber is quite low, it cannot be excluded that this band corresponds to the silent A_{1u} librational mode of the $P\bar{3}m1$ structure. The IR modes in figure 6 exhibit significantly different temperature dependence in the high- and low-temperature phases. In particular, the wavenumbers of nearly all IR modes increase with decreasing temperature in the high-temperature phase. Former Raman studies of $RbFe(MoO_4)_2$ showed the same behaviour for all Raman modes [13]. In the low-temperature phase, the wavenumbers of many IR modes decrease with decreasing temperature (figure 6). This behaviour is observed for all IR-active stretching modes of the MoO_4 units, and it was also observed previously for the totally symmetric Raman-active mode [13]. The increase of the wavenumber with decreasing temperature in the $P\bar{3}m1$ structure can be attributed to the fact that the MoO_4 units cannot rotate in this phase, since they are fixed by the mirror symmetry. The contraction of the unit-cell volume leads to a *decrease* of the interatomic distances and an increase of the wavenumber for the majority of phonon modes. As in the $P\bar{3}$ structure, the MoO_4 units are not fixed by symmetry: they can rotate about the threefold axis. This rotation causes significant changes in the bond angles and the interatomic distances. In particular, a comparison of the crystallographic data for the $P\bar{3}m1$ (at 295 K) and $P\bar{3}$ (at 110 K) structures shows that the Mo–O2 and Fe–O2 distances *increase* with decreasing temperature, whereas the Fe–O2–Mo bond angle significantly decreases. As a result, the wavenumbers of the stretching modes decrease with decreasing temperature below 190 K. It is worth noticing that the observed temperature dependence of the $RbFe(MoO_4)_2$ phonon wavenumbers below 190 K differs from what was previously observed by us for $KAl(MoO_4)_2$ [26]. In the latter case, the wavenumbers of the stretching modes did not decrease with decreasing temperature for the low-temperature phase. This difference clearly points to different mechanisms of the phase transitions in the two materials. A gradual tilt about the twofold axes occurs at the transition from $P\bar{3}m1$ to $C2/c$, $C2/m$, C_i or $P\bar{3}c$ structures, like in $KAl(MoO_4)_2$ and related scandium and indium double molybdates and tungstates [28]. On the other hand, the transition into the $P\bar{3}$ structure, like in $RbFe(MoO_4)_2$, is associated with a rotation about the threefold axis. Significant differences in the temperature dependence of the phonon modes for $KAl(MoO_4)_2$ and $RbFe(MoO_4)_2$ therefore support the conclusion that the low-temperature structure of $RbFe(MoO_4)_2$ is $P\bar{3}$ rather than $P\bar{3}c$, as previously suggested in [13].

3.5. High-pressure study

A series of high-pressure energy-dispersive x-ray diffraction spectra are shown in figure 7. Lattice parameters and unit-cell volumes were derived and refined from the positions of the Bragg peaks using the PURUM code [29]. The compression curve, i.e. the relative volume as a function of pressure, could then be described by the Murnaghan equation of state [30]:

$$P = \frac{B_0}{B_0'}(x^{-B_0'} - 1), \tag{1}$$

where the relative volume is denoted by $x = V/V_0$, V is the volume at pressure P and V_0 is the volume at zero pressure; B_0 and B_0' are the isothermal bulk modulus and its pressure derivative, both parameters evaluated at zero pressure. Values

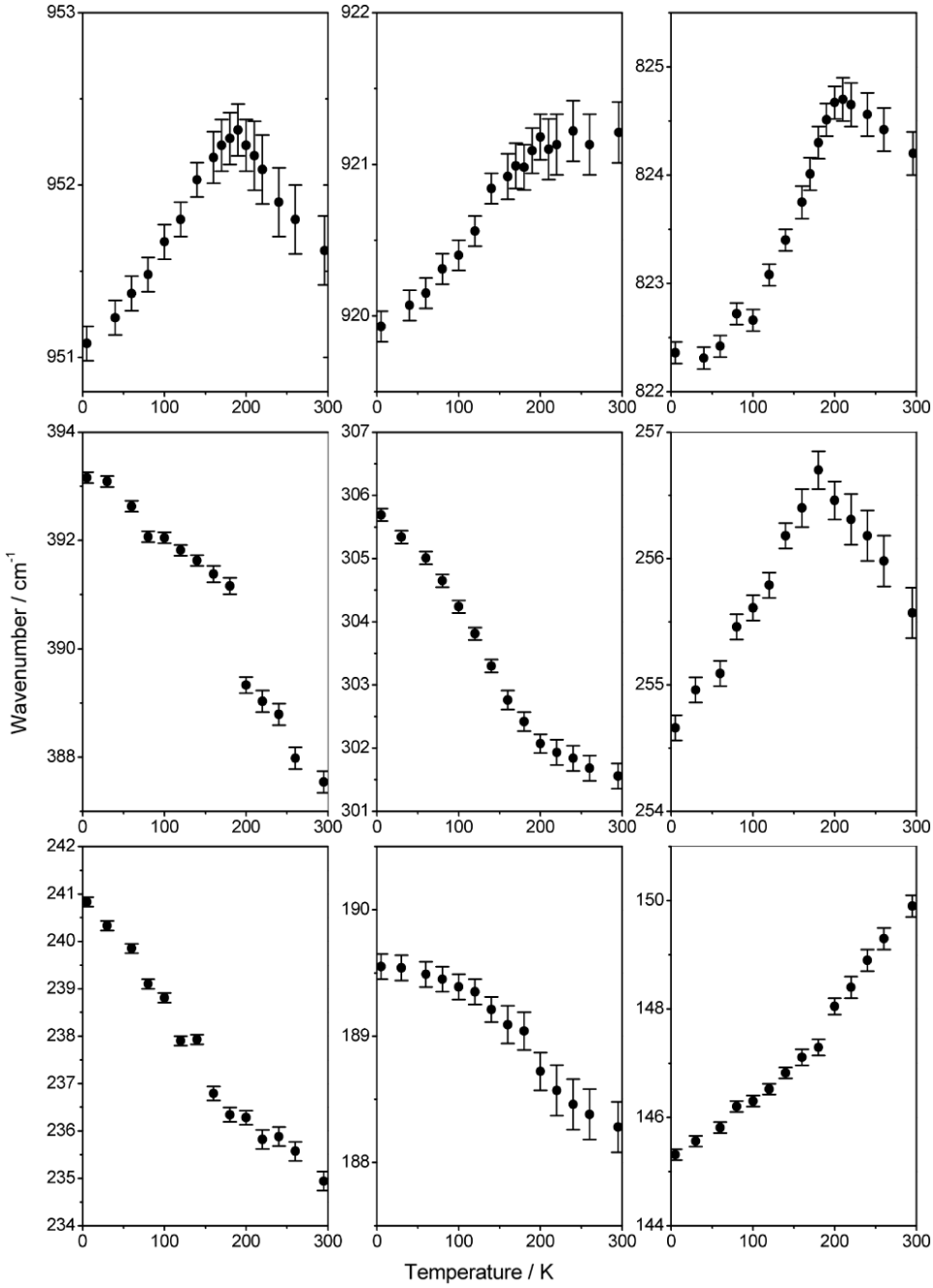

Figure 6. Vibrational wavenumbers (local maximum of absorption bands) versus temperature for $RbFe(MoO_4)_2$.

of B_0 and B_0' can be obtained from a nonlinear least-squares fit of equation (1) to the experimental P–V data.

The material is found to be extremely soft. A fit to the trigonal structure in the 0–5 GPa range gives the zero-pressure bulk modulus $B_0 = 7.89 \pm 0.60$ GPa, where the uncertainty is the standard error of the fit. This is a very small bulk modulus compared to what is typical for most solid materials. Thus, $RbFe(MoO_4)_2$ is a highly compressible material. In contrast, its pressure derivative has a rather high value, $B_0' = 9.98 \pm 1.05$, giving some stiffening at high pressure.

Computer simulated energy-dispersive spectra show that the expected diffraction patterns of space groups $P\bar{3}m1$ and $P\bar{3}$ are practically identical. Unfortunately, it is therefore impossible to distinguish these two phases in the x-ray diagrams. The observed variations in peak intensities are most probably due to preferred orientations of the material in the diamond-anvil pressure cell. An indication of a structural phase transformation above 5 GPa is the fact that the compression curve can be described by a single equation of state only up to 5 GPa (figure 8). The experimental pressure–volume data points would fall below the expected curve when extrapolating the equation of state beyond 5 GPa. There is also an increasing amorphization above 5 GPa (figure 7(b)), and at 12 GPa only weak diffraction lines remain on an

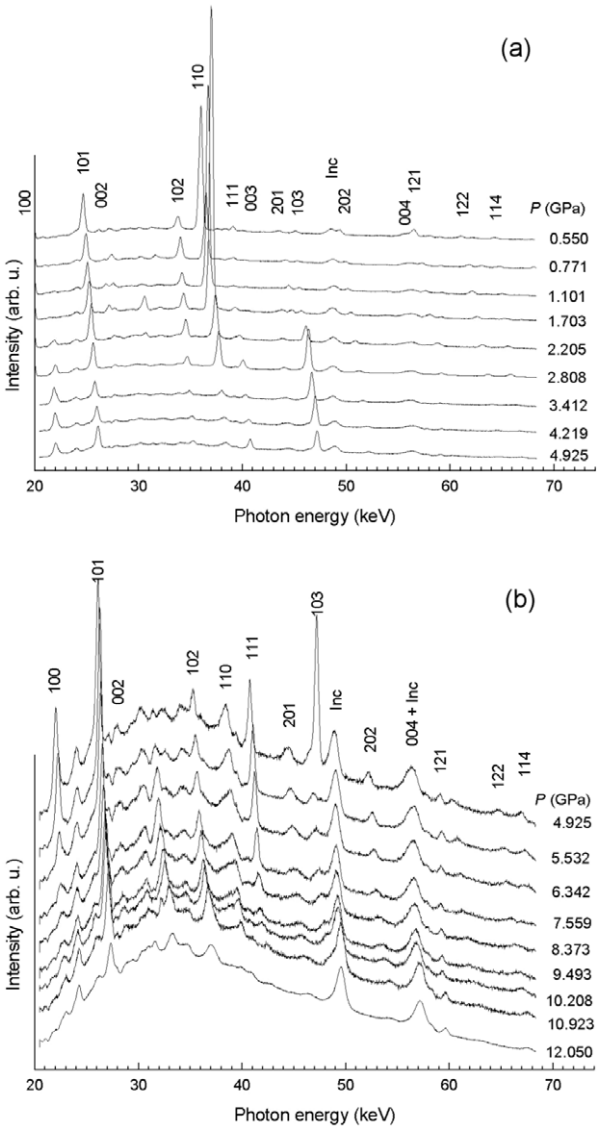

Figure 7. High-pressure energy-dispersive x-ray diffraction spectra. Bragg angle $\theta = 3.525°$. Inc = diffraction peak of the Inconel gasket. (a) $0.5 < P < 5$ GPa. At the lowest pressures, the 100 peak is hidden under the Mo Kβ peak at 19.61 keV outside the diagram. (b) $5 < P < 12$ GPa.

amorphous background. We speculate that above 5 GPa the Rb–O bond compression may gradually transform the structure into a topologically untenable form.

4. Summary

(i) Single crystals of $RbFe(MoO_4)_2$ have been prepared and their x-ray crystal structure determined at room temperature and 110 K in order to describe the structural modification induced by the phase transition at $T_c = 190$ K.

(ii) The temperature-dependent evolution of the unit cell is strongly anisotropic with marked discontinuity at T_c. The weak first-order character of the transition is consistent with the crystal symmetry change from $P\bar{3}m1$ to the non-isomorphous subgroup $P\bar{3}$.

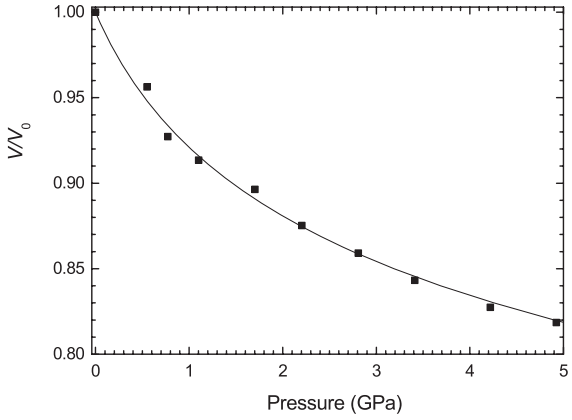

Figure 8. Relative volume, V/V_0, as a function of pressure in the range $0 < P < 5$ GPa. The solid curve is the least-squares fit of the Murnaghan equation (1) to the experimental pressure–volume data points.

(iii) The transition is of ferroelastic nature and its structural mechanism is mainly related to the strain-evoked displacements of O atoms in the crystallographic (a, b) plane. The O atoms' displacements cause in-phase rotations of the corner-sharing MoO_4 and FeO_6, which in turn lead to the distortion of the polyhedral layers arranged perpendicular to the c axis.

(iv) Temperature-dependent IR spectroscopy shows that the wavenumbers of all but one IR-active mode increase with decreasing temperature down to about 190 K. Below this temperature, the wavenumbers of many modes decrease with decreasing temperature. The observed IR behaviour is consistent with the results obtained by x-ray single-crystal diffraction and with the postulated symmetry change.

(v) The crystal is extremely soft with a high compressibility and a correspondingly low value of the bulk modulus $B_0 = 7.9(6)$ GPa. The rather large value of the pressure derivative $B_0' = 10(1)$ indicates that some stiffening occurs at high pressure. The high-pressure diffraction spectra can be indexed according to the trigonal structure up to about 5 GPa. Above this pressure, an onset of amorphization that increases on further pressure increase (up to 12 GPa) suggests the thermodynamic instability of the structure.

Acknowledgments

The authors wish to thank HASYLAB/DESY in Hamburg, Germany, for permission to use the synchrotron radiation facility. LG and JSO gratefully acknowledge financial support from the Danish Natural Sciences Foundation through DANSCATT.

References

[1] Klevtsova R F and Klevtsov P V 1970 *Kristallogr.* **15** 953–9 in Russian

[2] Klevtsov P V and Klevtsova R F 1977 *Zh. Struct. Khim.* **18** 419–39
[3] Bramwell S T, Carling S G, Harding C J, Harris K D M, Kariuki B M, Nixon L and Parkin I P 1996 *J. Phys.: Condens. Matter* **8** L123–9
[4] Inami T, Ajiro Y and Goto T 1996 *J. Phys. Soc. Japan* **65** 2374–6
[5] Serano-González H, Bramwell S T, Harris K D M, Kariuki B M, Nixon L, Parkin I P and Ritter C 1999 *Phys. Rev.* B **59** 14451–60
[6] Mączka M, Pietraszko A, Saraiva G D, Filho Souza A G, Paraguassu W, Lemos V, Perottoni C A, Gallas M R, Freire P T C, Tomaszewski P E, Melo F E A, Filho Mendes J and Hanuza J 2005 *J. Phys.: Condens. Matter* **17** 6285–6300
[7] Kenzelmann M, Lawes G, Harris A B, Gasparovic G, Broholm C, Ramirez A P, Jorge G A, Jaime M, Park S, Huang Q, Shapiro A Ya and Demianets L A 2007 *Phys. Rev. Lett.* **98** 267205
[8] Bazarov B G, Klevtsova R F, Bazarova C T, Glinskaya L A, Fedorov K N, Tsirendorzhiyeva A D, Chimitova O D and Bazarova Zh G 2006 *Zh. Neorganicheskoy Khimii* **51** 1190–4
[9] Wierzbicka-Wieczorek M, Kolitsch U and Tillmanns E 2009 *Z. Kristallogr.* **224** 151–62
[10] Svistov L E, Smirnov A I, Prozorova L A, Petrenko O A, Demianets L N and Shapiro A Ya 2003 *Phys. Rev.* B **67** 094434
[11] Prozorova L A, Svistov L E, Smirnov A I, Petrenko O A, Demianets L N and Shapiro A Ya 2003 *J. Magn. Magn. Mater.* **258/259** 394–7
[12] Jorge G A, Capan C, Ronning F, Jaime M, Kenzelmann M, Gasparovic G, Broholm C, Shapiro A Ya and Demianets L A 2004 *Physica* B **354** 297–9
[13] Klimin S A, Popova M N, Marvin B N, van Loosdrecht P H M, Svistov L E, Simonov A J, Prozorova L A, Krug von Nidda H-A, Seidov Z and Loidl A 2003 *Phys. Rev.* B **68** 174408
[14] Inami T 2007 *J. Solid State Chem.* **180** 2075–9
[15] Lawes G, Harris A B, Kimura T, Rogado N, Cava R J, Aharony A, Entin-Wolman O, Yildirim T, Kenzelmann M, Broholm C and Ramirez A P 2005 *Phys. Rev. Lett.* **95** 087205
[16] Picozzi S, Yamaguchi K, Sergeyenko I A, Sen C, Sanyal B and Dagotto E 2008 *J. Phys.: Condens. Matter* **20** 434208
[17] Oxford Diffraction 2001 *CrysAlis CCD, Data Collection Software* (Wrocław, Poland: Oxford Diffraction Ltd)
[18] Oxford Diffraction 2006 *CrysAlis RED, Data Reduction Program* (Wrocław, Poland: Oxford Diffraction Ltd) Issue 171.32
[19] Sheldrick G M 2008 SHELXL-97 *Acta Crystallogr.* A **64** 112–22
[20] Olsen J S 1992 *Rev. Sci. Instrum.* **83** 1058–61
[21] Mao H K, Xu J and Bell P M 1986 *J. Geophys. Res.* **91** 4673–6
[22] Herbst-Irmer R and Sheldrick G M 2002 *Acta Crystallogr.* B **58** 477–81
[23] Frazer B C and Brown P J 1962 *Phys. Rev.* **125** 1283–91
[24] Maczka M 1996 *Eur. J. Solid State Inorg. Chem.* **33** 783–92
[25] Maczka M, Hanuza J, Lutz E T G and Van der Maas J H 1999 *J. Solid State Chem.* **145** 751–6
[26] Maczka M, Hermanowicz K, Tomaszewski P E and Hanuza J 2004 *J. Phys.: Condens. Matter* **16** 3319–28
[27] Maczka M, Hanuza J, Kojima S and Van der Maas J H 2001 *J. Solid State Chem.* **158** 334–42
[28] Otko A I, Nesterenko N M and Povstyanyi L V 1978 *Phys. Status Solidi* A **46** 577
[29] Werner P-E 1969 *Arkiv Kemi* **31** 513–6
[30] Murnaghan F D 1951 *Finite Deformation of an Elastic Solid* (New York: Wiley)